Bottom-Up Synthesis of Anatase Nanoparticles with Graphene Domains

Gregory Mogilevsky,[†] Olga Hartman,[‡] Erik D. Emmons,[§] Alex Balboa,[‡] Jared B. DeCoste,[§] Bryan J. Schindler,[§] Ivan Iordanov,[‡] and Christopher J. Karwacki*,[‡]

[†]Booz Allen Hamilton, 4692 Millennium Drive, Belcamp, Maryland 21017, United States
[‡]Edgewood Chemical and Biological Center, 5183 Blackhawk Road, Gunpowder, Maryland 21010, United States
[§]Leidos, Inc., P.O. Box 68, Gunpowder, Maryland 21010, United States

Ⓢ *Supporting Information*

ABSTRACT: Using alizarin and titanium isopropoxide, we have succeeded in preparing a hybrid form of nanostructured graphene−TiO_2 following a bottom-up synthetic approach. This novel graphene-based composite offers a practical alternative to synthesizing photocatalytically active materials with maximized graphene−TiO_2 interface. The molecular precursor alizarin was chosen because it efficiently binds to TiO_2 through the hydroxyl groups and already possesses the graphene building block through its anthracene basis. XPS and Raman spectroscopy proved that the calcined material contained majority sp^2-hybridized carbon that formed graphene-like clusters. XRD data showed the integrated structures maintained their anatase crystallography, therefore preserving the material's properties without going through phase transitions to rutile. The enhanced graphene and TiO_2 interface was confirmed using DFT computational techniques. The photocatalytic activity of the graphene−TiO_2 materials was demonstrated through degradation of methylene blue.

KEYWORDS: graphene titania composite, new synthetic approach, enhanced interfacial contact, small organic precursor, bottom-up synthesis
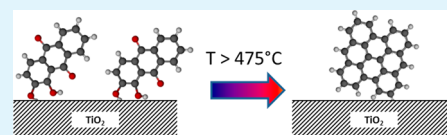
1. INTRODUCTION

Integrated graphene−TiO_2 (Gr−TiO_2) materials show great promise as photocatalysts and catalysts in many reactions.[1−7] The graphene domains in the hybrid structures enhance the intrinsic catalytic and photocatalytic properties of bare TiO_2 to improve the efficiency of the reactions.[2,6,8] The composite structure serves as an example of excellent use of graphene, a material with many unique properties. For example, in photocatalytic reactions graphene can serve as a hole or electron trap, slowing charge recombination in TiO_2, allowing the reaction to proceed more efficiently as compared to bare TiO_2.[9] Specifically, UV irradiation induces band gap excitation in TiO_2 followed by electron injection into the graphene clusters. This increases the excited lifetime of TiO_2, enabling more efficient photocatalytic reactions.[8]

It is still a topic of much research to find effective ways to synthesize integrated Gr−TiO_2 structures with the optimized interface. Creating the structure with maximized graphene−TiO_2 interface is motivated by the fact that the greatest enhancement of catalytic and photocatalytic properties of Gr−TiO_2 would occur when the interface between the graphene and the metal oxide is maximized, allowing an increased flux of charge transfer.[10] The Gr−TiO_2 material can be created by direct synthesis of exfoliated graphene sheets with TiO_2 to create a Gr−TiO_2 hybrid. This is typically done under vigorous ultrasonication, utilizing chemical surfactants to suspend the graphene. However, the surfactant additives react with the surface functional groups of the metal oxides while ultra-

sonication induces defects to the graphene structure, altering the electronic and surface properties of the material.[11,12] Another pathway to create graphene is chemical vapor deposition (CVD) where organic precursors in gaseous phase are cracked in temperatures ranging from 600−1000 °C on a metal catalyst to form controlled, uniform graphene films with excellent conductivity and large grain sizes.[13−15] However, anatase TiO_2 typically converts to less catalytically active rutile between 500 and 700 °C, lower than typical CVD conditions.[16]

Consider the organic dye alizarin (1,2-dihydroxy-9,10-anthracenedione), an anthracene derivative, as a precursor for graphene (see Figure 1). The molecule efficiently chemisorbs to the surface of TiO_2 through its hydroxyl functional groups.[17−19] Furthermore, alizarin is capable of forming a homogeneous solution with the TiO_2 precursor titanium isopropoxide in isopropanol, ensuring complete and total homogeneous mixture of the two precursors. Upon calcination,
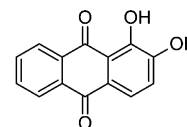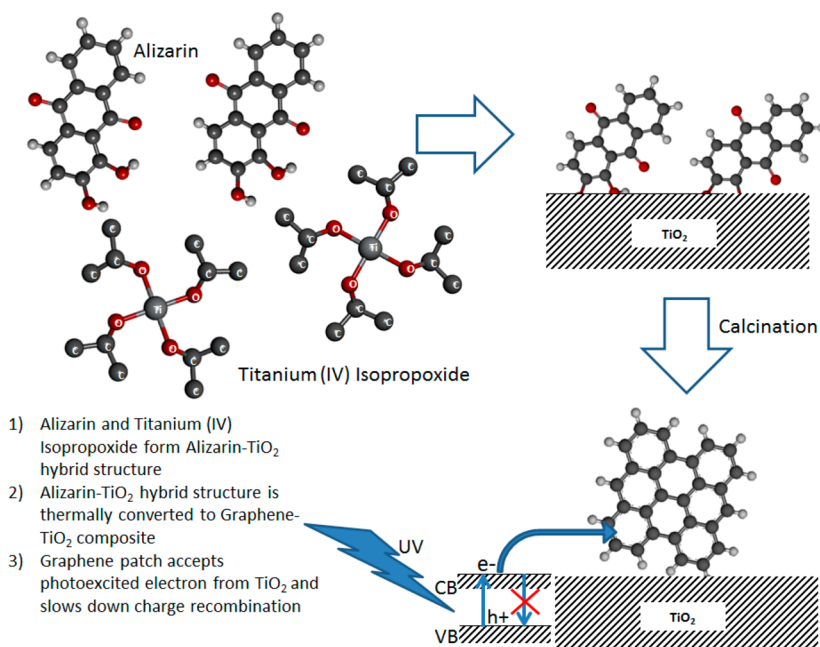

Figure 1. Structural formula of alizarin.

Scheme 1. Graphene Patch Formation from Alizarin

alizarin can convert into graphene clusters by thermal cyclodehydrogenation pathway,[20−22] which preserves the carbon sp^2 bond character of the anthracene backbone.

In this work, we developed a novel synthetic approach to grow integrated Gr−TiO$_2$ structures following a bottom-up synthesis and demonstrated their photocatalytic activity by photocatalytic degradation of methylene blue (MB) dye. The graphene component was grown from alizarin in situ with TiO$_2$ formation under increased thermal conditions (Scheme 1). We also perform density functional theory (DFT) calculations to confirm the binding properties of alizarin and graphene-like structures, conversion of alizarin to graphene patches, and their effect on resulting enhanced interface morphology and charge density.

We further show through DFT calculations that graphene patches within the Gr−TiO$_2$ material provide an electron acceptor site, into which photoexcited electrons from TiO$_2$ can inject. This slows the charge recombination, which would occur within the metal oxide in the absence of graphene. The slowing of charge recombination in the material allows for more efficient photocatalytic performance. As the graphene loading was increased in the current study, more active sites were introduced within the hybrid structure. The rate of MB degradation increased with higher loadings of alizarin. A more in-depth determination of the relationship and mechanism between electron injection into the graphene and kinetics is an ongoing effort. The bottom-up synthesis technique demonstrated in this work leads itself to the concept of rationally designed materials whose properties are controlled during the synthesis. This up-front synthesis control of the properties results in materials with tailored functionality.

2. EXPERIMENTAL SECTION

2.1. Preparation of TiO$_2$ and TiO$_2$−Alizarin Hybrid Powder by Sol−Gel Method. The metal oxide precursor solution was a mixture of 7 mL of titanium isopropoxide (TIP) (97%, supplied by Aldrich, U.S.) and 3 mL of isopropanol (IPA) (99%, supplied by Fisher Scientific, U.S.) combined to create an IPA/TIP solution. An 80 mL solution adjusted to pH = 12 using 35% NH$_4$OH, supplied by

Acros Organics, U.S., was added to the round-bottom flask that was placed on ice. Alizarin was purchased from Sigma-Aldrich, U.S., and served as a graphene precursor. For graphene formation studies, 0.2, 1, 2, and 5 wt % alizarin solutions were created in the IPA/TIP solution. The low concentration of alizarin was chosen to promote single layer graphene growth by avoiding π−π* stacking of the organic molecules in solution. Higher concentrations of the alizarin solution, with alizarin dimers and trimers, would cause formation of stacked layers of graphene. Samples with 1, 2, and 5 wt % alizarin were prepared for photocatalytic testing. The IPA/TIP solutions were slowly added into NH$_4$OH solution dropwise in ice for 30 min, while stirring. After the TIP/IPA solution was added in the pH solution, the round-bottom flask was transferred to a hot water bath (~90 °C) and stirred overnight for 24 h, resulting in suspensions of TiO$_2$ and alizarin−TiO$_2$ with different weight percentage loadings.

2.2. Hydrothermal Treatment. After being stirred overnight, the sol−gel solution was transferred to a 200 mL Teflon-lined autoclave. This autoclave was sealed and maintained at 130 °C for 24 h. The obtained white (bare TiO$_2$) or pink (alizarin−TiO$_2$) precipitates were collected on glass filter paper, washed thoroughly with distilled water, and then dried in a forced air oven at 65 °C for 24 h.

2.3. Graphitization of TiO$_2$−Alizarin Hybrid Powder. The Gr−TiO$_2$ nanocomposites were obtained by thermal reduction of alizarin−TiO$_2$ powder at 700 °C under a 100 mL/min flow of dry nitrogen. To establish the relationship between calcination temperature and resulting structures, the 0.2 wt % Gr−TiO$_2$ sample was heated to 475 and 700 °C, held at constant temperature for 30 min, and then cooled from the set point temperature to 25 °C for 1 h. For photocatalysis experiments, the samples were heated to 700 °C for 1 h, held at constant temperature for 30 min, and then cooled to 25 °C in 1 h. The temperature of 700 °C was chosen to strip selectively any carbonyl and hydroxyl groups off alizarin, leaving behind only the graphene-like anthracene backbone.[23] The TiO$_2$ samples containing graphitized alizarin for photocatalytic testing at different weight percentage loadings were designated 1.0 wt % Gr−TiO$_2$, 2.0 wt % Gr−TiO$_2$, and 5.0 wt % Gr−TiO$_2$. Similarly, TiO$_2$ containing no alizarin was thermally treated in a manner similar to the hybrid materials and was designated bare TiO$_2$.

Bulk alizarin (10 mg) was conditioned under the same temperature as the 1−5 wt % Gr−TiO$_2$ samples. Alizarin was calcined at 700 °C, under dry N$_2$ flow, for 30 min in a ceramic boat. Resulting black

10639

dx.doi.org/10.1021/am502322y | ACS Appl. Mater. Interfaces 2014, 6, 10638−10648

powder was analyzed with Raman spectroscopy to inform the structural properties.

2.4. Characterization. Bare TiO_2 and $Gr-TiO_2$ hybrid powders were characterized for their structural and morphological properties using the following techniques.

Powder X-ray diffraction (XRD) measurements were taken using a PANalytical X'Pert X-ray powder diffractometer with an X'celerator detector. Samples were scanned at 45 kV and 40 mA, using Cu Kα radiation ($\lambda = 1.54$ Å), a step size of $2\theta = 0.02°$ (5.0 s/step) over a range of $2\Theta = 5-80°$. Zero-background discs were used to minimize background scattering. XRD diffraction patterns were processed using the Reflex module in Material Studio 6.0 by Accelrys. The average crystallite size was determined by the broadening of the anatase (101) diffraction peak use the Debye–Scherrer equation.

The particle size and morphology of the powder were observed using a JEOL 6300F field emission scanning electron microscope (FESEM, JEOL, Japan) at an accelerating voltage of 200 kV. Average particle size for each sample calcined at different temperatures was determined using ImageJ software. Using the software, the average particle size was determined manually.

BET surface areas and pore size distributions were obtained by nitrogen adsorption isotherms at 77 K using a Quantachrome Autosorb-1. A relative pressure range of 10^{-4} to $p_{sat} = 1$ was measured for the adsorption branch followed by a desorption branch to indicate hysteresis. All samples were outgassed at 100 °C under vacuum for 20 h. BET specific surface areas (SSA) were derived from a linear region of the isotherm between relative pressures from 0.03 to 0.3 based on parameters described by Rouquerol et al. Pore size distributions were calculated using silica cylindrical pores NLDFT adsorption equilibria kernel.[24−26]

Raman spectra were recorded at room temperature using a JASCO NRS-3200 Raman microscope with a 532 nm frequency-doubled Nd:YAG laser. All spectra were acquired at ~10 mW laser power, with 1200 lines/mm grating (scan rate), 0.1 mm slit width, and 20−100 s integration time using 20× objective.

X-ray photoelectron spectroscopy (XPS) spectra were recorded using a PerkinElmer Phi 570 ESCA/SAM system employing Cu Kα X-rays. All binding energies are referenced to the carbon 1S photoelectron peak at 284.6 eV.

2.5. Computational Details. Ab initio calculations were performed using DFT with a plane wave basis set, as implemented in the Quantum Espresso code. The Perdew–Burke–Ernzerhof (PBE) functional[27] was used to treat the exchange and correlation potentials. The core electrons were approximated through ultrasoft pseudopotentials, while the energy cutoff for the plane wave basis set was set at 37 Ry. The interface between TiO_2 and graphene is modeled within a periodic vacuum slab model, with a vacuum region of ~15 Å. A (101) surface of TiO_2 was cleaved and used in the calculations. Two layers of TiO_2 are used (thickness ~10 Å), below a single sheet of graphene. The size of the cell is $20.4 \times 7.6 \times 30.8$ Å, with a total of 204 atoms, 60 carbons for the graphene and 48 Ti and 96 O for TiO_2.

2.6. Photocatalytic Measurement. The photocatalytic activities of bare TiO_2 and 1.0%, 2.0%, and 5.0 wt % alizarin loaded $Gr-TiO_2$ samples were tested with a methylene blue (MB) aqueous solution. A stock solution of 9.75×10^{-5} M MB in deionized Milli-Q water was used for all experiments. A 100 W 365 nm lamp was used to irradiate the stirred MB in solution with bare TiO_2 or with $Gr-TiO_2$ powders for a predetermined time period. The MB solution was stirred with the different wt % catalyst powder until adsorption equilibrium was achieved prior to UV irradiation to deconvolute as much as possible the effect of MB adsorption from photocatalytic degradation. An Agilent Hewlett-Packard 8453A UV−vis−NIR spectrophotometer was used to measure the intensity of the supernatant MB solution after UV exposure. Over time, the decrease in the 609 nm UV−vis band's signal intensity of the solution was correlated to the decrease of MB concentration. To calibrate the instrument's absorbance signal intensity to concentration of the MB solution, controlled diluted MB solutions were generated, analyzed with UV−vis, and calibrated to a concentration value.

3. RESULTS AND DISCUSSION

3.1. Synthesis and Characterization of TiO_2 and $Gr-TiO_2$ Structures. XRD confirmed that the TiO_2 component of the composite preserves its anatase structure and size. We also confirmed that the resulting material's size remains constant after temperature treatments. This is important because particles grown to larger sizes due to thermally induced ripening were shown to lose their catalytic properties.[28]

We prepared the TiO_2 in alkaline conditions because high pH synthesis allowed the anatase nanoparticles to retain their structure at 700 °C (see the discussion and Figure S1 in the Supporting Information for comparison of thermal structural response of low pH and high pH synthesized TiO_2). The XRD patterns of all of the samples synthesized at 700 °C are shown in Figure 2.
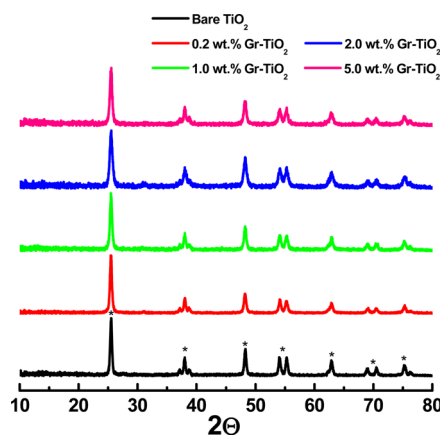
Figure 2. XRD patterns of bare TiO_2 and $Gr-TiO_2$ materials calcined at 700 °C, pH = 12. *Anatase peaks.

The figure shows XRD patterns of bare TiO_2 along with $Gr-TiO_2$ loaded with 0.2, 1.0, 2, and 5 wt % alizarin. The anatase structure is preserved in all materials even at 700 °C. This suppression of rutile formation was previously observed in TiO_2 crystals that were coated with graphite.[29] No graphene spectrum is observed in any spectra within Figure 2. This is likely because the low (0.2−5 wt %) loading of alizarin does not yield any stacked graphene sheets that would provide an XRD response. It is anticipated that the sizes of individual graphene clusters formed from alizarin are smaller than graphene formed by graphene oxide reduction methods, where the structure is based on large graphene patches scattered with TiO_2 nanoparticles.[1,6,9] This is due to the fact that thermal cyclodehydrogenation reactions of small aromatic molecules typically produce small graphene clusters.[21] Overloading a graphene−TiO_2 nanocomposite with multiple layers of graphene actually lowers the photocatalytic performance of the material because excess graphene hinders contact between the analyte and TiO_2, lowering photocatalytic performance.[8] Additionally, previous work concluded that graphene−TiO_2 hybrid materials with low graphene loadings from 0.1 to 5 wt % all improved upon the photocatalytic performance of bare TiO_2,[6,30] with the desired charge transport properties of graphene observed in graphitic structures as small as 1.7 nm.[31]

The size of the TiO_2 crystallites can be approximated by using the Debye−Scherrer equation, which determines the length of a crystalline domain in a specific crystallographic direction. To compare the relative sizes of the crystals calcined

at different temperatures, we choose the length in the [101] direction, which corresponds to the XRD peak at $2\theta \approx 25°$. The Debye−Scherrer lengths in the [101] direction presented in Table 1 indicate that the individual crystallites grow as the

**Table 1. Bare TiO$_2$ and 0.2 wt % Gr−TiO$_2$ Crystal Size Following Thermal Treatment**

sample	mean crystal size[a] (nm)
TiO$_2$-130	32.6
TiO$_2$-475	34.7
TiO$_2$-700	47.9
Gr−TiO$_2$-130	29.9
Gr−TiO$_2$-475	34.7
Gr−TiO$_2$-700	44.8

[a]Referenced to the (101) surface.

calcination temperature is increased, as expected. The addition of alizarin does not change the crystallographic properties of the TiO$_2$ nanoparticles such as size and crystal structure. The sizes of the crystalline domains of TiO$_2$ and 0.2 wt % Gr−TiO$_2$ remain similar at all temperatures. Therefore, presumably, the anatase structure of TiO$_2$ is preserved.

Morphological properties of the materials were further studied by SEM (Figure 3). SEM images indicate that the
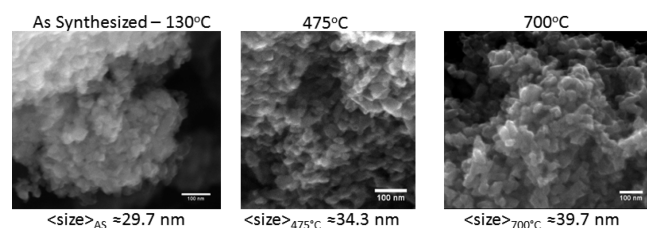
Figure 3. SEM images of 0.2 wt % Gr−TiO$_2$ structures.

material is made of nanoparticles, forming aggregates. The average size of individual nanoparticles in the aggregates was measured from the SEM images and found to confirm the results as indicated by the XRD Debye−Scherrer calculations. Table 2 shows the textural properties derived from the nitrogen isotherms on bare TiO$_2$ and 0.2 wt % Gr−TiO$_2$ samples for thermal treatments at 130, 475, and 700 °C.

For the bare TiO$_2$ materials, we determined that the majority of pore widths for the lower temperature treated materials (130 and 475 °C) were estimated to be 5.0 nm with total pore volume spanning 0.309 to 0.165 mL/g. At 700 °C, the structure had undergone a dramatic contraction, resulting in a volume

Table 2. Textural Properties of TiO$_2$ (Bare) and 0.2 wt % Gr−TiO$_2$ at Different Temperature Treatments

samples	SSA$_{BET}$ (m^2/g)	D$_p$[a] (nm)	V$_{micro}$[b] (mL/g)	V$_{total}$ (mL/g)
TiO$_2$-130	351.6	5.0	0.291	0.309
TiO$_2$-475	150.6	5.0	0.149	0.165
TiO$_2$-700	27.0	13.9	0	0.089
Gr−TiO$_2$-130	88.4	17.3	0	0.376
Gr−TiO$_2$-475	92.9	17.3	0	0.368
Gr−TiO$_2$-700	59.9	17.3	0	0.263

[a]Pore width calculated by NLDFT silica-equilibrium adsorption kernel (ref Quantachrome). [b]Micropore volume determined by t-method.

(V_{total}) decrease to 0.089 mL/g. Furthermore, the calculated mean pore width, determined from a NLDFT silica-equilibrium adsorption kernel, increased to 13.9 nm at 700 °C. Over this temperature range (130−700 °C), the calculated specific surface area (SSA$_{BET}$) of bare TiO$_2$ decreased from 351.6 to 27.0 m^2/g. The temperature-sensitive change in TiO$_2$ morphology is likely related to the slight growth of TiO$_2$ crystals, as discussed above and summarized in Table 1. For the 0.2 wt % Gr−TiO$_2$ materials, there was an apparent and dramatic disruption in the formation of mesopores resulting in a lower volume distributed over a pore size ranging from about 5.0 to 25.0 nm (see Figure 4; x-axis shown in angstroms). For
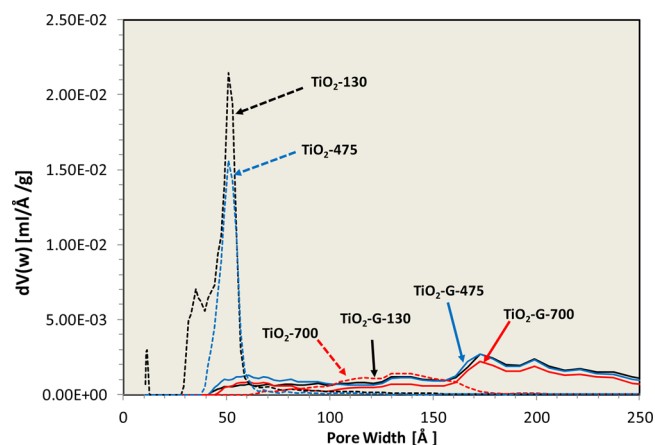
Figure 4. Pore size distribution for TiO$_2$ (bare) and 0.2 wt % Gr−TiO$_2$ samples thermally treated at 130, 475, and 700 °C. Estimated pore volumes derived from a DFT-SiO$_2$ adsorption kernel.

these materials, the total pore volume ranged from 0.376 (130 °C) to 0.263 (700 °C) mL and occupied a mean pore width of 17.3 nm. The calculated specific SSA$_{BET}$ remained relatively stable with temperature treatment resulting in values ranging from 88.4−59.9 m^2/g.

Although a precise understanding has yet to be developed, it is possible a strong affinity between alizarin and TiO$_2$ is affecting formation of micropores to a greater extent than the development of crystal size. A comparison of the TiO$_2$ and 0.2 wt % Gr−TiO$_2$ for each temperature treatment shows virtually no change in the crystal size (TiO$_2$ 32.6−47.6 nm and Gr−TiO$_2$ 29.9−44.8 nm) upon addition of alizarin and its transformation to graphene. The limiting effect on TiO$_2$ crystal size may be an indication of the approximate dimensions of the alizarin/graphene "patch". At the as-synthesized temperature, 130 °C, there is an immediate effect on porosity upon addition of the alizarin to TiO$_2$ resulting in about a 75% reduction in specific surface area (S_{BET}: 351 for TiO$_2$-130 to 88.4 m^2/g for Gr-TiO$_2$-130); however, the total pore volume (V_t: 0.309−0.376 mL/g) remains. At higher temperatures, 475 and 700 °C, there is a small change in porosity for the TiO$_2$ (BET 150.6 and 27.0 m^2/g, respectively) and Gr−TiO$_2$ (BET 92.2 and 59.9 m^2/g, respectively) materials, indicating that alizarin and its transformation to graphene appear to have a stabilizing effect on the hybrid structure. A key factor in the formation of microporous TiO$_2$ is related to the environment governing assembly of the colloidal phase. Moreover, the origin of micro- and mesopore development is influenced by early formation of surface hydroxyl groups, which upon heating and dehydration form a polycrystalline phase with characteristic pore dimen-
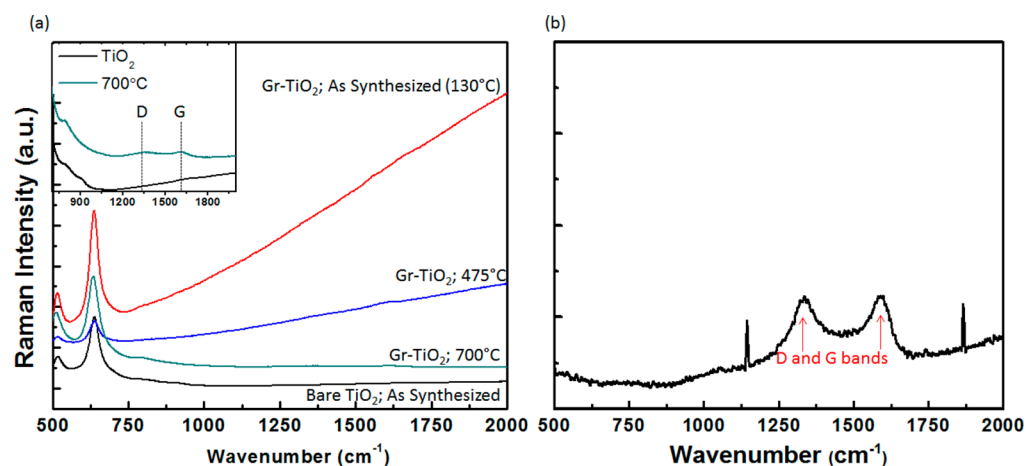
10641

dx.doi.org/10.1021/am502322y | ACS Appl. Mater. Interfaces 2014, 6, 10638−10648

Figure 5. Raman spectra of (a) bare TiO$_2$, 0.2 wt % Gr−TiO$_2$ at 130, 475, and 700 °C; and (b) pure alizarin calcined at 700 °C.

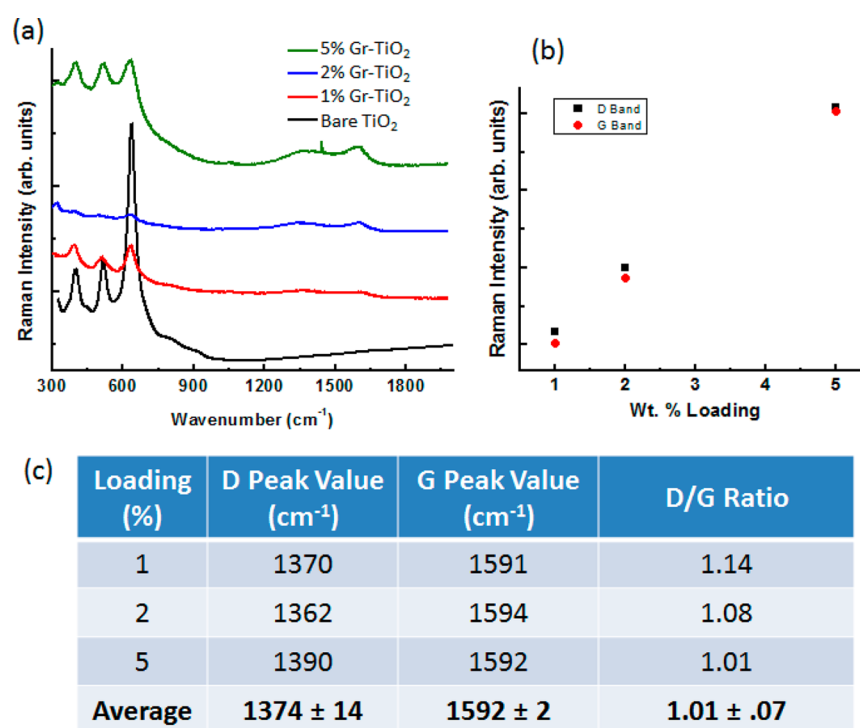| Loading (%)	D Peak Value (cm^{-1})	G Peak Value (cm^{-1})	D/G Ratio
1	1370	1591	1.14
2	1362	1594	1.08
5	1390	1592	1.01
Average	1374 ± 14	1592 ± 2	1.01 ± .07

Figure 6. Raman spectra and peak analysis of 1.0−5.0 wt % Gr−TiO$_2$-700 samples used in photocatalysis tests. (a) Raman spectra of 1.0−5.0 wt % Gr−TiO$_2$ samples, (b) D and G peak intensities graphed against weight loading of alizarin, and (c) table showing properties of D and G peaks in 1.0−5.0 wt % Gr−TiO$_2$ samples.
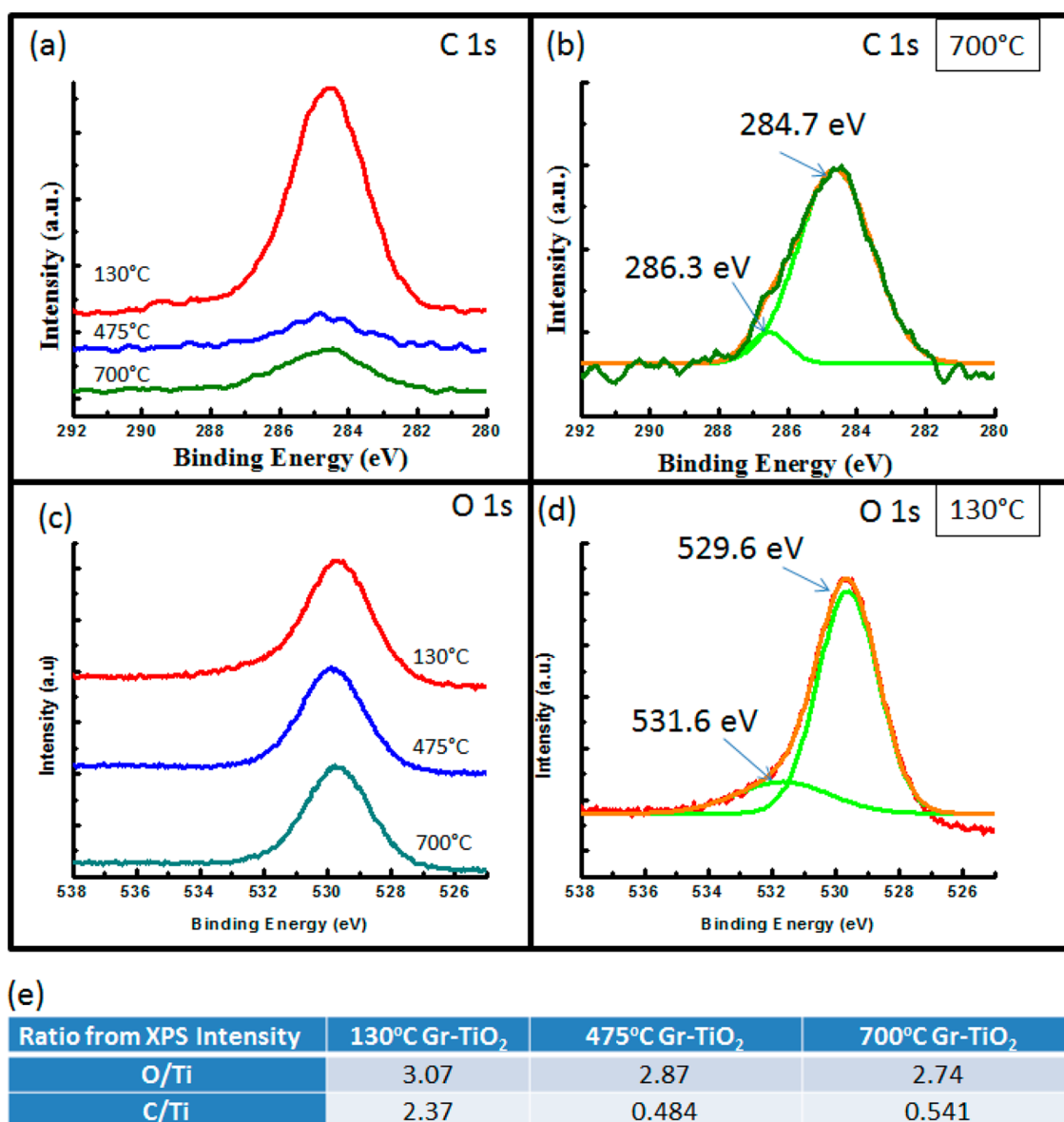
sions. The addition of organic precursors, such as alizarin, likely interferes with cross-linking of surface hydroxyl groups by hydrogen bonding.

3.2. Characterization of the Graphene Domains. Raman spectroscopy and XPS are commonly used together to identify and characterize specific structures in composite materials. Here, they are used complementary to identify the precise structure of the carbon present in the hybrid materials. Raman spectra of graphitic materials feature peaks at approximately 1350 and 1590 cm^{-1}, corresponding to the D and G bands, respectively. The intensity and shift of the D band are indicative of disorder, whereas the intensity and shift of the G band are indicative of sp^2 carbon amount and morphology.[32−36]

Figure 5a shows the Raman spectra for bare TiO$_2$ and 0.2 wt % Gr−TiO$_2$ materials calcined at 130, 475, and 700 °C. The

spectrum of as-synthesized 130 °C 0.2 wt % Gr−TiO$_2$ features peaks corresponding to anatase and unreacted alizarin, along with a strong fluorescent background.[37] This is expected because alizarin is a dye molecule with a large molar extinction coefficient, which luminesces upon excitation at 532 nm.[38−40] In the 475 °C spectrum, the characteristic graphene D and G bands start taking shape, but the spectrum also includes a fluorescence signal. This is because at this temperature not all surface-bound alizarin converts to graphene. Therefore, the residual, ungraphitized alizarin molecules produce a fluorescent background similar to the 130 °C sample. Finally, the Raman spectrum of the alizarin loaded TiO$_2$ sample calcined at 700 °C only shows graphene D and G peaks at 1350 and 1603 cm^{-1}, respectfully, without any fluorescence background. The D and G peak values at 532 nm excitation wavelength correspond to those of nanosized graphene-like carbon rather than bulk

(e)

Ratio from XPS Intensity	130°C Gr-TiO$_2$	475°C Gr-TiO$_2$	700°C Gr-TiO$_2$
O/Ti	3.07	2.87	2.74
C/Ti	2.37	0.484	0.541

Figure 7. (a) C 1s XPS spectra of 0.2 wt % Gr−TiO$_2$ samples calcined at 130, 475, and 700 °C; (b) deconvoluted C 1s XPS spectrum of 0.2 wt % Gr−TiO$_2$ at 700 °C; (c) O 1s XPS spectrum of 0.2 wt % Gr−TiO$_2$ as-synthesized calcined at 130, 475, and 700 °C; (d) deconvoluted O 1s XPS spectrum of 0.2 wt % Gr−TiO$_2$ prepared at 130 °C; and (e) ratios of peak intensities for 0.2 wt % Gr−TiO$_2$.

graphite.[41] Lack of fluorescence and emergence of the D and G peaks are indicative of total conversion of the molecular precursors to graphene domains.

To confirm that alizarin indeed thermally converts to graphene-like carbon structures with majority sp^2 bonds when adsorbed on TiO$_2$ rather than graphite, alizarin alone was calcined in a ceramic boat under dry N$_2$ flow at 700 °C. It was expected that alizarin molecules convert to multilayer graphite, composed of randomly oriented graphitic sheets, in the presence of a chemical vacuum. The calcined alizarin spectrum (Figure 5b) features the D and G peaks at 1330 and 1580 cm^{-1}. The G peak wavenumber value of the graphitized alizarin is red-shifted from the G peak value of 1603 cm^{-1} of the 700 °C calcined Gr−TiO$_2$ in Figure 5a. This is because upon calcination at 700 °C in a chemical vacuum (dry N$_2$ flow), raw alizarin indeed forms multilayer graphite. The G band location of graphite is lower than 1600 cm^{-1}.[35] On the other hand, the low wt % amount of alizarin on TiO$_2$ forms clusters

whose structure closer resembles single-layer graphene. This is because the concentration of alizarin is chosen to be small, such that no dimers or trimers are formed in solution and alizarin deposits on TiO$_2$ as single molecules. Therefore, when calcined, individual, single molecules of alizarin convert to graphene clusters. The subtle difference in G peak values has been observed using Raman spectroscopy, where single layer graphene's G-band is always blue-shifted (higher wavenumber value) from that of graphite.[34]

Raman spectroscopy further confirms graphene formation by monitoring the formation of D and G peaks and their relative intensities with higher loadings of graphene. Figure 6 shows the Raman analysis of the higher loaded Gr−TiO$_2$ samples treated at 700 °C. Figure 6a plots all Raman spectra for the higher loaded samples together. The D and G graphene bands grow linearly as the loading of alizarin is increased (Figure 6b). The corresponding wavenumber values of the D and G peaks remain at 1374 ± 8 and 1591.9 ± 0.9 cm^{-1}, respectively at all

loadings along with the D/G peak height ratio remaining at 1.01 ± 0.07 (Figure 6c). The G peak value is blue-shifted from the G peak of calcined alizarin and remains within the range of graphene, rather than graphite. The Raman analysis provides evidence that nanocrystalline graphene clusters are formed throughout the anatase crystals for all alizarin loadings, not graphite.[33,35]

To provide further evidence of graphene-like structure of the carbon species on TiO$_2$, XPS was used to elucidate the type of bonding that occurs on the surface. XPS peaks are able to discern between different types of carbon or oxygen bonds in the material and provide a relative amount of species containing those bonds. XPS was collected of all Gr−TiO$_2$ samples, calcined at different temperatures, and compared to bare TiO$_2$. The spectra in Figure 7a show XPS of the C 1s binding energies for the 0.2 wt % Gr−TiO$_2$ material prepared at 130, 475, and 700 °C. The 130 °C prepared 0.2 wt % Gr−TiO$_2$ sample shows a large XPS peak at 284.7 eV, which corresponds to a combination of sp^2 bonded carbons and other carbonaceous species, that come from alizarin and ligands in the precursor titanium isopropoxide material, respectively.[5,30]

The samples that were calcined at 475 and 700 °C demonstrated a decrease in C1 peak intensities. This is likely caused by the evaporation and decomposition of any weakly surface-bound carbon species, at the higher temperatures generated by the tube furnace during calcination, introduced by residual oxygen impurities in the carrier gas. The spectrum of the 700 °C sample is deconvoluted and shown in Figure 7b. The spectrum is composed of two peaks, a major one at 284.7 eV and a minor one at 286.3 eV. The 284.7 eV peak corresponds to sp^2-hybridized carbons, C−C, as confirmed by Raman spectrometry, because the observed surface-bound carbon groups possess G and D bands.[30] The 286.3 eV peak likely come from sp^2-hybridizid defects and sp^3-hybridized C−C and C−H bonds.[30,42] The ratio of the 286.3 eV peak to the 284.7 eV peak is 0.08, indicating that the majority of contributing signal comes from defect-free sp^2 bonded carbon. C 1s XPS results combined with the Raman spectroscopy results, which show the G and D bands, further confirm that the majority of carbon structure on the TiO$_2$ surface converted to graphene.

The O 1s XPS data in Figure 7c and d on the calcined samples provide further details on the graphitization process. Qualitatively, the total intensity of the O 1s spectra does not change with calcination, indicating that the majority of oxygen in the sample comes from lattice TiO$_2$ rather than from any organic ligand. The table in Figure 7e shows that as the temperature increases, the O/Ti ratio decreases from 3.07 in the 130 °C 0.2 wt % Gr−TiO$_2$ to 2.74 in the 700 °C 0.2 wt % Gr−TiO$_2$ material. The XPS spectrum of bare TiO$_2$ (not shown) produces the O/Ti ratio of 2.43, which is close to the ideal O/Ti ratio of 2 as expected in pure TiO$_2$. The 3.07 ratio for as-synthesized Gr−TiO$_2$ comes from oxygen contributions of alizarin, oxide, and any residual precursor material. As the temperature increases, alizarin loses its oxygens and converts to graphene, lowering the O/Ti ratio of Gr−TiO$_2$. As the temperature increases from 475 to 700 °C, the O/Ti ratio further decreases from 2.87 to 2.74, and the C/Ti ratio increases from 0.484 to 0.541. This provides quantitative evidence that with the increase of calcination temperature, alizarin loses its oxygen and hydroxyl groups and leaves behind only carbon.

Finally, the deconvoluted O 1s XPS spectrum in Figure 7d reveals more information on the fate of oxygen-containing species in the Gr−TiO$_2$ sample, as the sample is thermally treated. The peak at 531.6 eV corresponds to the carbonyl O=C bond, likely coming from alizarin.[43,44] The peak at 529.6 eV corresponds to the lattice oxygen in TiO$_2$.[44] As temperature increases, the 531.6 eV peak decreases and only the 529.6 eV remains, indicating that any remaining oxygen content in the structure comes from lattice oxygen in the TiO$_2$. This further supports that the organic components on the surface of the TiO$_2$ convert to graphene because graphene domains will not contain oxygen. Similar XPS analysis was performed on the 700 °C calcined 5 wt % loaded Gr−TiO$_2$ sample used for photocatalytic experiments (Supporting Information, Figure S2).

3.3. Computational Results. The DFT calculations of the graphene/TiO$_2$ system confirmed the enhanced interfacial contact between graphene and TiO$_2$. As seen in the SEM images in Figure 3, the agglomeration of TiO$_2$ nanoparticles (NPs) results in numerous pores in the ~5 nm size range with NPs on the order of 30 nm (see Tables 1 and 2). These characteristics persist unless the particles are heated to 700 K, resulting in larger particles (~40 nm) and much fewer, larger pores. The addition of TiO$_2$ to the graphene also eliminates the ~5 nm sized pores, but does so without significantly changing the nanoparticle sizes. A natural assumption then is that graphene has filled up the small pores or otherwise changed the NP/NP interface. We have used DFT calculations to test these assumptions, as well as generally improve our understanding of the TiO$_2$/graphene interface. Similar models have been used previously to model TiO$_2$/graphene interfaces; however, the majority of theoretical work has been focused on the (110) surface of rutile.[45−47] Here, we focus on the (101) anatase surface, most commonly found in our experiment. We find that graphene has a relatively weak interaction with TiO$_2$ of about 0.06 eV/atom (Table 3). Because it is expected that the

Table 3. Effect of Oxygenation on the Binding Energy to TiO$_2$ of a Full Graphene Sheet

proportion of oxygenated carbons	total binding energy (eV)
0	1.23
0.0164	1.02
0.0667	0.372
0.25	0.353
1	0.785

graphene in the present experiments is not pristine, calculations were also done with partial and full-oxygenated carbons (Table 3). The addition of oxygen appears to weaken the binding further. This is most likely due to oxygen causing puckering or bending in the graphene sheet, and hence nonoptimal carbon−TiO$_2$ distance for many carbon atoms.

To simulate the relatively small graphene patches on and between TiO$_2$ NP's, we have also modeled a case where one-half of the graphene is removed from the calculation cell, thus effectively simulating an infinite ribbon with a finite width. The binding energy per atom of the ribbons decreased to ~0.01 eV/atom, about one-half of the binding energy to a full graphene sheet. We also examined the effect of adding O and OH groups on the surface and edges of the graphene ribbons (Table 4). Adding O and OH groups to the ribbon strengthens the binding to the TiO$_2$ surface. The precise location of the groups

10644

dx.doi.org/10.1021/am502322y | ACS Appl. Mater. Interfaces 2014, 6, 10638−10648

Table 4. Binding Energies of Graphene Ribbons with Additional Groups

added group	binding energy (eV)
none	0.341
3O	0.381
3OH	0.558
5OH + 2O	0.780

on graphene and the alignment relative to the surface can have a nontrivial effect in these calculations. A full accounting of all possible configurations of O and OH on the surface is beyond the scope of this work. However, because all of the binding energies of the various configurations that were examined remain below 1 eV for a 30 atom sheet, in this case we do not expect that functionalization with O and OH will lead to qualitatively different behavior.

We also examined how graphene embeds between TiO_2 NPs by gradually lowering the length of vacuum in the cell, effectively simulating the case where graphene is positioned in a channel between two TiO_2 NPs. We found that the energy is minimized at a cell length of 18.2 Å. At this cell size, the binding energy of the graphene is 0.52 eV, slightly less than double the amount when there is a sizable (~15 Å) vacuum gap with a ~30 Å cell size. Because of the stronger binding, one can expect graphene to prefer to be bound in the small nanopores between individual TiO_2 nanoparticles. This would effectively fill the pores in the material, as seen experimentally (Table 2).

DFT calculations of alizarin's binding to anatase reveal what one might have expected, that the interaction is primarily due to a hydrogen bond between one of the hydroxyl groups and a TiO_2 surface oxygen (Figure 8). An interesting finding from this calculation is that in this type of bonding, other hydroxyl groups on the alizarin molecule rearrange themselves to create a hydrogen bond-like interaction with the lone oxygen on
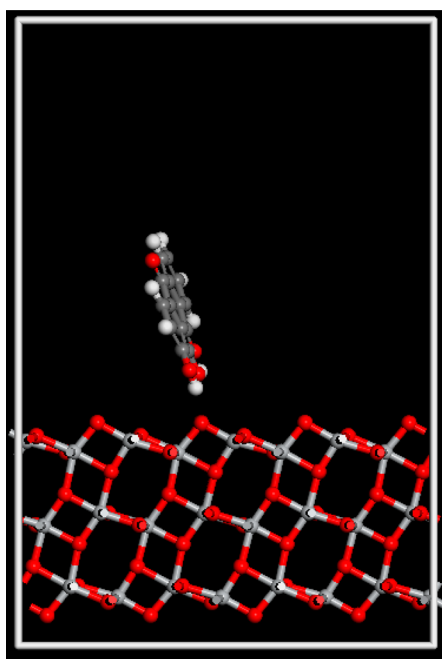

Figure 8. Alizarin bound to TiO_2 in the vertical orientation. Binding energy is 1.42 eV in shown orientation, and 1.33 eV for flat orientation.

alizarin. This rearrangement is easy to miss when optimizing the structure, and yet it lowers the binding energy by about ~0.8 eV. Calculations of alizarin oriented vertically and flat relative to the surface only differed by 0.1 eV. This suggests that alizarin is only bound to the surface through a single hydrogen bond and the rest of the molecule can rotate relatively freely. Even though the absolute binding energy of a sheet of graphene is on the same order of magnitude as alizarin, because the binding of alizarin to TiO_2 is through a single strong bond, we can expect alizarin to be much harder to remove from TiO_2. Given the 1.2 eV binding energy and the experimental conditions used, approximately one monolayer coverage, 600−900 K temperature range, we do not expect significant desorption during the calcination process. This would mean that alizarin remains on the surface through the calcination process, converting to graphene patches on the surface.
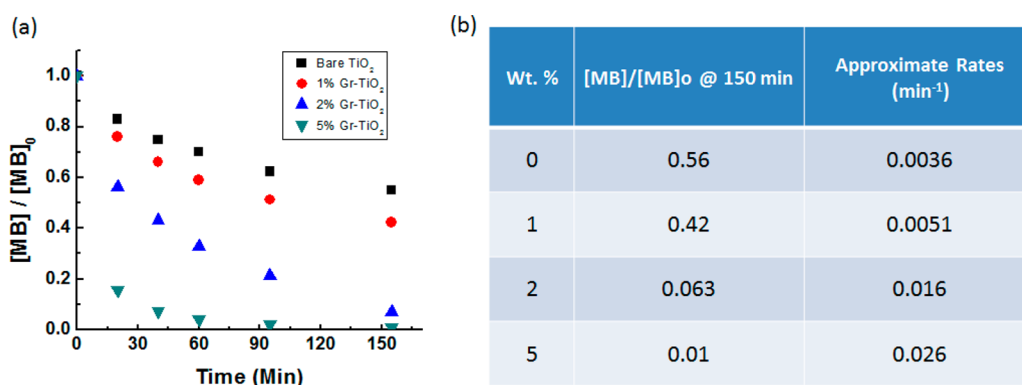
Another issue of particular interest for a photoactive material such as TiO_2 is the degree of charge transfer that occurs after photoexcitation at the interface with graphene. As an example, calculations of this type have been used to characterize the silica/graphene interface, among others.[48,49] We have explored the amount of charge transfer through charge density difference plots. For these calculations, the charge density is calculated for graphene/TiO_2 together and then for graphene and TiO_2 separately, but in the exact same cell and position. We then take the difference between the combined charge density and the two individual charge densities of TiO_2 and graphene, resulting in a 3D plot of the charge density difference due to the interface. To focus on the charge transfer between planes, the charge difference plots are planar averaged within the bottom plane of the cell (in the plane of the graphene surface). This results in a 1D graph of charge difference per unit length in the direction normal to the surfaces at the interface (Figure 9). The 1D graph allows us to see the movement of electrons away from, or toward, the graphene at the interface. We observe a transfer of electrons from graphene to the oxygens in the top layer of TiO_2 when the graphene patch is brought in contact with the TiO_2 surface. These results were also confirmed for the graphene ribbons and for the case where graphene is effectively sandwiched by TiO_2 on both sides by the elimination of the vacuum region. The charge difference density is a measure of the planar integrated change in charge density due to the interaction of the two substrates. Positive in this case means the addition of electrons (negative charge), and negative denotes the removal of electrons (positive charge). There is clear charge transfer from graphene to the top oxygen layer of TiO_2, meaning graphene is left positively charged and TiO_2 is negative. The total charge transfer is on the order of 0.017 e$^-$ per carbon atom.

3.4. Photocatalytic Activity. To demonstrate the photocatalytic activity of the Gr−TiO_2 material, and show its potential as a rationally designed functional material, the three weight loadings (1.0, 2.0, and 5.0 wt % Gr−TiO_2) of the hybrid structure were compared to bare TiO_2 to degrade the organic dye methylene blue (MB). The three loadings are expected to show progressive enhancement of MB degradation kinetics, illustrating how precise tailoring of the material's properties leads to a change in its performance. Figure 10 shows the residual concentration of MB of the Gr−TiO_2 samples with time, as compared to bare TiO_2. The individual photocatalysis UV−vis results at each time step, for all TiO_2 loadings, are shown in the Supporting Information (Figure S3). The residual C/Co ratios at 150 min for each graphene loading are
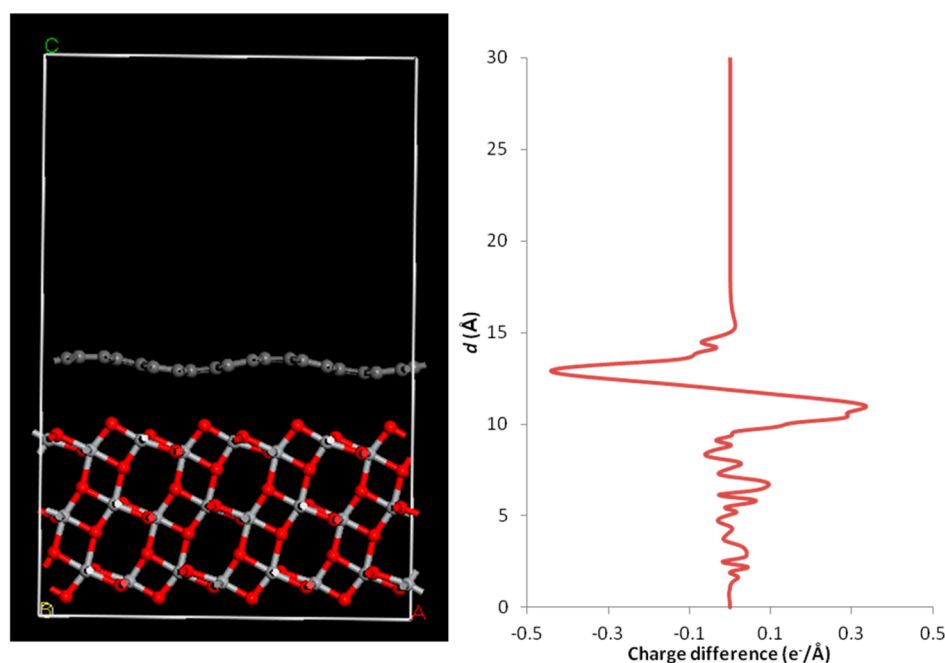
Figure 9. Model cell alongside with the planar averaged charge difference. d(Å) is the position on the z-axis of the unit cell (the one normal to the graphene/TiO$_2$ surfaces) and the y-axis of the graph on the right side of the figure.

Wt. %	[MB]/[MB]o @ 150 min	Approximate Rates (min^{-1})
0	0.56	0.0036
1	0.42	0.0051
2	0.063	0.016
5	0.01	0.026

Figure 10. Evaluation of MB degradation over time by plotting intensity of the 609 nm absorbance peak. (a) Concentration of MB plotted against time of UV irradiation, exposed to Gr−TiO$_2$. (b) Table showing remaining concentration of MB after 150 min and corresponding degradation rates.

presented in the table in Figure 10b. At 150 min, TiO$_2$ alone decomposes MB to 56%. As graphene is added to TiO$_2$ during synthesis, the residual MB concentration lowers after 150 min of reaction, implying less residual MB in solution.

The rate of MB degradation was estimated to first-order kinetics to provide a qualitative approximation of the effect of graphene loading (Supporting Information, Figure S4). The approximate first-order rate constants of MB degradation increase from 0.0036 to 0.026 min^{-1} (Figure 10b). Although the rate is derived from first-order kinetics, it is important to note that the kinetics are not necessarily completely first order. The reduction of residual MB in solution is believed to be a combination of at least two overlapping phenomena including photocatalytic degradation of MB, along with adsorption of the molecule to the graphene domains through $\pi-\pi$ interactions. Without a thorough examination of reaction products after 150 min of UV light exposure, it is impossible to determine whether the reduction of MB from solution is due to adsorption, photocatalytic degradation, or a combination of both. To test the role of UV light in the reaction, we left the MB in solution

stirring for 150 min in the presence of bare TiO$_2$ absent any irradiation. We observed a minimal decrease of MB concentration over the 150 min span (see the Supporting Information, Figure S5), confirming that UV irradiation enhanced the degradation of the molecule. Additionally, any adsorption effect will aid in photocatalysis because the adsorbed species will be in close contact with the catalyst material for more efficient reactivity.

The data analysis presented in Figure 10 clearly shows a trend where up to 5 wt % loading the nanocomposite's photocatalytic performance is increased with the addition of graphene clusters. As more graphene is loaded onto the surface, this inhibits recombination through more paths for photo-excited electrons and holes to inject into the graphene clusters, prolonging the photoexcited state. The prolonged photoexcited state allows for a more efficient photocatalytic reaction. Ongoing studies are exploring the mechanism, kinetics, and loading dependence in detail. However, these preliminary results indicate that the bottom-up approach allows for the

control of a material's properties as the material's performance can be tailored at the very beginning of the synthesis process.

4. CONCLUSION

Integrated Gr—TiO₂ structures were synthesized following a bottom-up route starting with precursor molecules alizarin and titanium isopropoxide. The approach produced a material with TiO₂ and graphene in intimate contact because the precursor molecules formed a stable, homogeneous phase. The precursor alizarin was chosen such that it intimately binds to TiO₂ through the hydroxyl groups and already possesses the graphene building block through its anthracene backbone. A low concentration of the precursor was chosen to minimize the deposition of alizarin dimers, which would have caused multiple layers of graphene to form. XPS and Raman spectroscopy showed that the material contained majority sp^2-hybridized carbon that formed graphene-like clusters. The XRD study indicated that TiO₂ maintained its anatase crystallography in the integrated structure, therefore preserving the material's properties without going through a phase transition to rutile. Furthermore, the method does not induce crystal growth through ripening, because XRD and SEM show that the nanoparticles remained the same size throughout the calcination process. The bonding of alizarin and graphene patches was studied using DFT calculations, to give more insight on the mechanism. It was found that alizarin binds to the TiO₂ surface and there is a driving force for the calcined graphene patches to remain on the surface. In addition, the DFT calculations showed how the morphology of the material changed due to the graphene patches propensity to remain on the surface and create a driving force to accept electrons from TiO₂. Finally, the material was shown to be active in photocatalytic decomposition of MB dye under UV irradiation.

■ ASSOCIATED CONTENT

Ⓢ Supporting Information

Further details including pH and thermal dependency of the hybrid materials, further XPS results, photocatalysis UV−vis results, and kinetic approximations. This material is available free of charge via the Internet at http://pubs.acs.org.

■ AUTHOR INFORMATION

Corresponding Author

*Tel.: (410) 436-5704. Fax: (410) 436-5513. E-mail: christopher.j.karwacki.civ@mail.mil.

Notes

The authors declare no competing financial interest.

■ ACKNOWLEDGMENTS

■ REFERENCES

(1) Du, J.; Lai, X.; Yang, N.; Zhai, J.; Kisailus, D.; Su, F.; Wang, D.; Jiang, L. Hierarchically Ordered Macro-Mesoporous TiO₂-Graphene Composite Films: Improved Mass Transfer, Reduced Charge Recombination, and their Enhanced Photocatalytic Activities. *ACS Nano* **2011**, *5*, 590−596.

(2) Kamat, P. V. Graphene-Based Nanoarchitectures. Anchoring Semiconductor and Metal Nanoparticles on a Two-Dimensional Carbon Support. *J. Phys. Chem. Lett.* **2010**, *1*, 520−527.

(3) Lettmann, C.; Hildenbrand, K.; Kisch, H.; Macyk, W.; Maier, W. F. Visible Light Photodegradation of 4-Chlorophenol with a Coke-Containing Titanium Dioxide Photocatalyst. *Appl. Catal., B* **2001**, *32*, 215−227.

(4) Morales-Torres, S.; Pastrana-Martínez, L. M.; Figueiredo, J. L.; Faria, J. L.; Silva, M. T. Design of Graphene-Based TiO₂ Photo-catalysts - a Review. *Environ. Sci. Pollut. Res.* **2012**, *19*, 3676−3687.

(5) Sun, L.; Zhao, Z.; Zhou, Y.; Liu, L. Anatase TiO₂ Nanocrystals with Exposed 001 Facets on Graphene Sheets Via Molecular Grafting for Enhanced Photocatalytic Activity. *Nanoscale* **2012**, *4*, 613−620.

(6) Zhang, H.; Lv, X.; Li, Y.; Wang, Y.; Li, J. P25-Graphene Composite as a High Performance Photocatalyst. *ACS Nano* **2010**, *4*, 380−386.

(7) Zhong, J.; Chen, F.; Zhang, J. Carbon-Deposited TiO₂: Synthesis, Characterization, and Visible Photocatalytic Performance. *J. Phys. Chem. C* **2009**, *114*, 933−939.

(8) Štengl, V.; Popelková, D.; Vlacil, P. TiO₂-Graphene Nano-composite as High Performace Photocatalysts. *J. Phys. Chem. C* **2011**, *115*, 25209−25218.

(9) Zhang, Y.; Tang, Z.; Fu, X.; Xu, Y. TiO₂-Graphene Nano-composites for Gas-Phase Photocatalytic Degradation of Volatile Aromatic Pollutant: Is TiO₂-Graphene Truly Different from Other TiO₂-Carbon Composite Materials? *ACS Nano* **2010**, *4*, 7303−7314.

(10) Zhang, Y.; Zhang, N.; Tang, Z.; Xu, Y. Improving the Photocatalytic Performance of Graphene-TiO₂ Nanocomposites Via a Combined Strategy of Decreasing Defects of Graphene and Increasing Interfacial Contact. *Phys. Chem. Chem. Phys.* **2012**, *14*, 9167−9175.

(11) Paredes, J. I.; Villar-Rodil, S.; Martinez-Alonso, A.; Tascon, J. M. D. Graphene Oxide Dispersions in Organic Solvents. *Langmuir* **2008**, *24*, 10560−10564.

(12) Melcarne, G.; De Marco, L.; Carlino, E.; Martina, F.; Manca, M.; Cingolani, R.; Gigli, G.; Ciccarella, G. Surfactant-Free Synthesis of Pure Anatase TiO₂ Nanorods Suitable for Dye-Sensitized Solar Cells. *J. Mater. Chem.* **2010**, *20*, 7248−7254.

(13) Li, X.; Cai, W.; An, J.; Kim, S.; Nah, J.; Yang, D.; Piner, R.; Velamakanni, A.; Jung, I.; Tutuc, E.; Banerjee, S. K.; Colombo, L.; Ruoff, R. S. Large-Area Synthesis of High-Quality and Uniform Graphene Films on Copper Foils. *Science* **2009**, *324*, 1312−1314.

(14) Li, X.; Cai, W.; Colombo, L.; Ruoff, R. S. Evolution of Graphene Growth on Ni and Cu by Carbon Isotope Labeling. *Nano Lett.* **2009**, *9*, 4268−4272.

(15) Li, X.; Magnuson, C. W.; Venugopal, A.; An, J.; Suk, J. W.; Han, B.; Borysiak, M.; Cai, W.; Velamakanni, A.; Zhu, Y.; Fu, L.; Vogel, E. M.; Voelkl, E.; Colombo, L.; Ruoff, R. S. Graphene Films with Large Domain Size by a Two-Step Chemical Vapor Deposition Process. *Nano Lett.* **2010**, *10*, 4328−4334.

(16) Hanaor, D.; Sorrell, C. Review of the Anatase to Rutile Phase Transformation. *J. Mater. Sci.* **2011**, *46*, 855−874.

(17) Di Iorio, Y.; Brusa, M.; Feldhoff, A.; Grela, M. Electron Transfer from Photoexcited TiO₂ to Chelating Alizarin Molecules: Reversible Photochromic Effect in Alizarin @ TiO₂ Under UV Irradiation. *ChemPhysChem* **2009**, *10*, 1077−1083.

(18) Duncan, W. R.; Prezhdo, O. V. Electronic Structure and Spectra of Catechol and Alizarin in the Gas Phase and Attached to Titanium. *J. Phys. Chem. B* **2005**, *109*, 365−373.

(19) Duncan, W. R.; Prezhdo, O. V. Nonadiabatic Molecular Dynamics Study of Electron Transfer from Alizarin to the Hydrated Ti⁴⁺ Ion. *J. Phys. Chem. B* **2005**, *109*, 17998−18002.

(20) Schwab, M. G.; Narita, A.; Hernandez, Y.; Balandina, T.; Mali, K. S.; De Feyter, S.; Feng, X.; Mullen, K. Structurally Defined Graphene Nanoribbons with High Lateral Extension. *J. Am. Chem. Soc.* **2012**, *134*, 18169−18172.

(21) Diev, V. V.; Schlenker, C. W.; Hanson, K.; Zhong, Q.; Zimmerman, J. D.; Forrest, S. R.; Thompson, M. E. Porphyrins Fused with Unactivated Polycyclic Aromatic Hydrocarbons. *J. Org. Chem.* **2012**, *77*, 143−159.

(22) Cai, J.; Ruffieux, P.; Jaafar, R.; Bieri, M.; Braun, T.; Blankenburg, S.; Muoth, M.; Seitsonen, A. P.; Saleh, M.; Feng, X.; Mullen, K.; Fasel, R. Atomically Precise Bottom-Up Fabrication of Graphene Nanoribbons. *Nature* **2010**, *466*, 470−473.

(23) Figueiredo, J. L.; Pereira, M. F. R.; Freitas, M. M. A.; Órfão, J. J. M. Modification of the Surface Chemistry of Activated Carbons. *Carbon* **1999**, *37*, 1379−1389.

(24) Ravikovitch, P. I.; Neimark, A. V. Density Functional Theory Model of Adsorption on Amorphous and Microporous Silica Materials. *Langmuir* **2006**, *22*, 11171−11179.

(25) Rouquerol, J.; Llewellyn, P.; Rouquerol, F. Is the BET Equation Applicable to Microporous Adsorbents? *Studies in Surface Science and Catalysis*; Elsevier: New York, 2007; Vol. *160*, pp 49−56.

(26) Landers, J.; Gor, G. Y.; Neimark, A. V. Density Functional Theory Methods for Characterization of Porous Materials. *Colloids Surf., A* **2013**, *427*, 3−32.

(27) Perdew, J. P.; Burke, K.; Ernzerhof, M. Generalized Gradient Approximation made Simple. *Phys. Rev. Lett.* **1996**, *77*, 3865−3868.

(28) Jassby, D.; Farner Budarz, J.; Wiesner, M. Impact of Aggregate Size and Structure on the Photocatalytic Properties of TiO_2 and ZnO Nanoparticles. *Environ. Sci. Technol.* **2012**, *46*, 6934−6941.

(29) Zhang, L.; Fu, H.; Zhu, Y. Efficient TiO2 Photocatalysts from Surface Hybridization of TiO2 Particles with Graphite-Like Carbon. *Adv. Funct. Mater.* **2008**, *18*, 2180−2189.

(30) Liu, S.; Liu, C.; Wang, W.; Cheng, B.; Yu, J. Unique Photocatalytic Oxidation Reactivity and Selectivity of TiO_2-Graphene Nanocomposites. *Nanoscale* **2012**, *4*, 3193−3200.

(31) Langlais, V. J.; Schlittler, R. R.; Tang, H.; Gourdon, A.; Joachim, C.; Gimzewski, J. K. Spatially Resolved Tunneling Along a Molecular Wire. *Phys. Rev. Lett.* **1999**, *83*, 2809−2812.

(32) Dresselhaus, M. S.; Jorio, A.; Hofmann, M.; Dresselhaus, G.; Saito, R. Perspectives on Carbon Nanotubes and Graphene Raman Spectroscopy. *Nano Lett.* **2010**, *10*, 751−758.

(33) Ferrari, A. C.; Robertson, J. Interpretation of Raman Spectra of Disordered and Amorphous Carbon. *Phys. Rev. B* **2000**, *61*, 14095−14107.

(34) Ferrari, A. C. Raman Spectroscopy of Graphene and Graphite: Disorder, Electron−Phonon Coupling, Doping and Nonadiabatic Effects. *Solid State Commun.* **2007**, *143*, 47−57.

(35) Casiraghi, C.; Ferrari, A. C.; Robertson, J. Raman Spectroscopy of Hydrogenated Amorphous Carbons. *Phys. Rev. B* **2005**, *72*, 085401.

(36) Ferrari, A. C.; Robertson, J. Resonant Raman Spectroscopy of Disordered, Amorphous, and Diamondlike Carbon. *Phys. Rev. B* **2001**, *64*, 075414.

(37) Shoute, L. C. T.; Loppnow, G. R. Excited-State Dynamics of Alizarin-Sensitized TiO_2 Nanoparticles from Resonance Raman Spectroscopy. *J. Chem. Phys.* **2002**, *117*, 842−850.

(38) Huber, R.; Sporlein, S.; Moser, J. E.; Gratzel, M.; Wachtveitl, J. The Role of Surface States in the Ultrafast Photoinduced Electron Transfer from Sensitizing Dye Molecules to Semiconductor Colloids. *J. Phys. Chem. B* **2000**, *104*, 8995−9003.

(39) Huber, R.; Moser, J.; Gratzel, M.; Wachtveitl, J. Real-Time Observation of Photoinduced Adiabatic Electron Transfer in Strongly Coupled Dye/Semiconductor Colloidal Systems with a 6 Fs Time Constant. *J. Phys. Chem. B* **2002**, *106*, 6494−6499.

(40) Di Iorio, Y.; Rodriguez, H. B.; San Roman, E.; Grela, M. A. Photoelectrochemical Behavior of Alizarin Modified TiO_2 Films. *J. Phys. Chem. C* **2010**, *114*, 11515−11521.

(41) Chen, C.; Wang, L.; Liu, Y.; Chen, Z.; Pan, D.; Li, Z.; Jiao, Z.; Hu, P.; Shek, C.; Wu, C. M. L.; Lai, J. K. L.; Wu, M. Assembling Tin Dioxide Quantum Dots to Graphene Nanosheets by a Facile Ultrasonic Route. *Langmuir* **2013**, *29*, 4111−4118.

(42) Luo, Z.; Shang, J.; Lim, S.; Li, D.; Xiong, Q.; Shen, Z.; Lin, J.; Yu, T. Modulating the Electronic Structures of Graphene by Controllable Hydrogenation. *Appl. Phys. Lett.* **2010**, *97*, 233111.

(43) Kumar, A. S.; Sornambikai, S.; Gayathri, P.; Zen, J. Selective Covalent Immobilization of Catechol on Activated Carbon Electrodes. *J. Electroanal. Chem.* **2010**, *641*, 131−135.

(44) Chen, L.; Chen, F.; Shi, Y.; Zhang, J. Preparation and Visible Light Photocatalytic Activity of a Graphite-Like Carbonaceous Surface Modified TiO2 Photocatalyst. *J. Phys. Chem. C* **2012**, *116*, 8579−8586.

(45) Long, R.; English, N. J.; Prezhdo, O. V. Photo-Induced Charge Separation Across the Graphene-TiO2 Interface is Faster than Energy Losses: A Time-Domain Ab Initio Analysis. *J. Am. Chem. Soc.* **2012**, *134*, 14238−14248.

(46) Du, A.; Ng, Y. H.; Bell, N. J.; Zhu, Z.; Amal, R.; Smith, S. C. Hybrid Graphene/Titania Nanocomposite: Interface Charge Transfer, Hole Doping, and Sensitization for Visible Light Response. *J. Phys. Chem. Lett.* **2011**, *2*, 894−899.

(47) Ayissi, S.; Charpentier, P. A.; Farhangi, N.; Wood, J. A.; Palotas, K.; Hofer, W. A. Interaction of Titanium Oxide Nanostructures with Graphene and Functionalized Graphene Nanoribbons: A DFT Study. *J. Phys. Chem. C* **2013**, *117*, 25424−25432.

(48) Romero, H. E.; Shen, N.; Joshi, P.; Gutierrez, H. R.; Tadigadapa, S. A.; Sofo, J. O.; Eklund, P. C. N-Type Behavior of Graphene Supported on Si/SiO2 Substrates. *ACS Nano* **2008**, *2*, 2037−2044.

(49) Ding, M.; Tang, Y.; Star, A. Understanding Interfaces in Metal-Graphitic Hybrid Nanostructures. *J. Phys. Chem. Lett.* **2013**, *4*, 147−160.

■ NOTE ADDED AFTER ASAP PUBLICATION

This paper was published on the Web on June 27, 2014, with errors in the Supporting Information file. The corrected version was reposted on July 9, 2014.

10648

dx.doi.org/10.1021/am502322y | *ACS Appl. Mater. Interfaces* 2014, 6, 10638−10648